

So You Want to Image Myelin Using MRI: Magnetic Susceptibility Source Separation for Myelin Imaging

Jongho Lee^{1+*}, Sooyeon Ji¹⁺, Se-Hong Oh^{2*}

Department of Electrical and Computer Engineering, Seoul National University, Seoul, Korea, Republic of¹

Biomedical Engineering, Hankuk University of Foreign Studies, Yongin, Korea, Republic of²
+ are the co-first authors, * are the co-corresponding authors

Corresponding authors

Jongho Lee, PhD

Department of Electrical and Computer Engineering, Seoul National University, Seoul, Korea, Republic of

Phone: +82-2-880-7310

Email: jonghoyi@snu.ac.kr

Se-Hong Oh, PhD

Department of Biomedical Engineering, Hankuk University of Foreign Studies, Yongin, Korea, Republic of

Phone: +82-31-330-4592

Email: jakeoh79@gmail.com

Running Title: Susceptibility Source Separation for Myelin

Key words

Myelin imaging, Magnetic susceptibility source separation, Chi-separation or χ -separation, Quantitative susceptibility mapping (QSM), Myelin water imaging (MWI)

ORCID

Jongho Lee (0000-0002-9485-5434), Sooyeon Ji (0000-0003-1644-6560), Se-Hong Oh (0000-0001-9771-8382)

Abstract

In MRI, researchers have long endeavored to effectively visualize myelin distribution in the brain, a pursuit with significant implications for both scientific research and clinical applications. Over time, various methods such as myelin water imaging, magnetization transfer imaging, and relaxometric imaging have been developed, each carrying distinct advantages and limitations. Recently, an innovative technique named as magnetic susceptibility source separation has emerged, introducing a novel surrogate biomarker for myelin in the form of a diamagnetic susceptibility map. This paper comprehensively reviews this cutting-edge method, providing the fundamental concepts of magnetic susceptibility, susceptibility imaging, and the validation of the diamagnetic susceptibility map as a myelin biomarker that indirectly measure myelin content. Additionally, the paper explores essential aspects of data acquisition and processing, offering practical insights for readers. A comparison with established myelin imaging methods is also presented, and both current and prospective clinical and scientific applications are discussed to provide a holistic understanding of the technique. This work aims to serve as a foundational resource for newcomers entering this dynamic and rapidly expanding field.

Abbreviations

MS: multiple sclerosis

fMRI: functional MRI

SWI: susceptibility weighted imaging

QSM: quantitative susceptibility mapping

GRE: gradient recalled echo

SE: spin echo

LFB: luxol fast blue

ROI: region of interest

MWI: myelin water imaging

UTE: ultra-short echo time

NMO: neuromyelitis optica

Introduction

The central nervous system, an intricate network of neurons and glia, relies on a pivotal player – myelin – to orchestrate rapid and precise neural communication. Myelin, composed of a lipid bilayer membrane, envelops axons, forming a protective sheath. Its high cholesterol content, which reflects and scatters light, contributes to the distinct white appearance of the brain's white matter. The functional significance of myelin lies in its ability to insulate nerve fibers, preventing signal loss and facilitating saltatory conduction. In MRI, the distinct properties of myelin make it a key determinant in multiple MRI contrasts observed between white and gray matter (e.g., T₁-weighted image, T₂-weighted image, and susceptibility), offering invaluable insights into the brain structure, function and pathology.

Because of its value in clinic and neuroscience, the pursuit of myelin-specific imaging methods has been a long-standing objective in MRI. Various techniques, including myelin water imaging (MWI),¹⁻⁴ magnetization transfer imaging and its variations,⁵⁻⁸ diffusion imaging,⁹ myelin volume fraction from synthetic MRI,^{10,11} and other relaxometry imaging,¹¹⁻¹⁸ have been developed as biomarkers that provide sensitivity and specificity to myelin. More recently, magnetic susceptibility imaging^{19,20} has been proposed, leveraging the diamagnetic susceptibility characteristics of myelin.^{21,22} While each method aims to serve as a biomarker for myelin, they come with inherent advantages and limitations.²³⁻²⁸ Consequently, the field is characterized by ongoing efforts to develop novel contrast mechanisms and refine existing methods, reflecting the continuous quest for myelin-specific imaging.

These myelin imaging methods have found a number of applications in neuroscience and clinical research. For example, they have been utilized to create the myeloarchitecture of the neocortex,^{13,16,29-35} that has an important value in cortical parcellation. The studies of myelin change during development³⁶⁻⁴⁶ and normal aging⁴⁷⁻⁴⁹ have also been conducted using myelin imaging, revealing age-dependent myelin concentration changes. More recently, the methods have been applied for the studies of brain plasticity, suggesting training-induced myelin changes.^{50,51} In clinical research, the techniques have been applied for various neurological disorders including multiple sclerosis (MS)⁵²⁻⁵⁷ and leukodystrophy.⁵⁸⁻⁶¹ In particular, MS where loss of myelin is the hallmark of the disease, has been the target of the myelin

imaging methods, exploring diagnosis,^{62–64} lesion characterization,^{52,53,65–68} disease progression monitoring,^{69–71} and treatment assessment.⁷²

In this review, we will delve into the technique of advanced magnetic susceptibility imaging for myelin imaging.⁷³ This relatively new field, coined as magnetic susceptibility source separation,^{35,64,73–84} presents a novel avenue for generating an indirect measure of myelin information in both gray and white matter of the brain, overcoming some of the limitations associated with traditional myelin-specific imaging approaches. By employing an advanced biophysical model and leveraging the diamagnetic susceptibility characteristics of myelin, the susceptibility source separation aims to provide high-resolution quantitative myelin information. In this review, we navigate the landscape of this emerging technique, exploring its fundamental physics, elucidating both advantages and challenges inherent in this approach. Our scope extends to considerations of data acquisition and processing, providing commentary on the current and potential applications of this novel method in the quest to map myelin distribution in the brain. The structure of this review is formed in nine questions and answers with some overlap among the answers. Finally, we hope you have an opportunity to gain an overview of this emerging and rapidly growing technique of magnetic susceptibility source separation.

Question 1: Let me begin with basic questions. What is susceptibility and how does it affect MRI?

Answer 1: Magnetic susceptibility is the degree to which a material is magnetized in response to an applied magnetic field. This can be expressed as $B = \mu H = \mu_0(1 + \chi)H$ for a linear and isotropic material, where B is the magnetic field experienced by the material, μ is magnetic permeability of the material, μ_0 is the magnetic permeability of vacuum, χ is the magnetic susceptibility of the material, and H is the applied field. For example, if a sphere of deoxygenated hemoglobin proteins is placed in water in a magnetic field (H -field), the sphere will experience a higher field than water (B -field) because the deoxygenated hemoglobin has higher susceptibility ($\chi = +0.15$ ppm)⁸⁵ than that of water ($\chi = -9.05$ ppm)⁸⁵ (Figure 1a). Note that the field change is not confined to the sphere. Depending on the sign of χ , we categorize a material as diamagnetic if χ is negative (e.g., cholesterol: $\chi = -9.23$ ppm)⁸⁶, paramagnetic if χ is small positive (e.g., ferritin: $\chi = 520$ ppm)⁸⁵ or ferromagnetic if χ is large positive. In MRI, we do not scan ferromagnetic materials due to safety and artifacts,⁸⁵ limiting the materials of interest to para-

and diamagnetic materials. Although this categorization relative to the susceptibility of vacuum ($\chi = 0$ ppm) is universal, many MRI literature uses water susceptibility as the reference.^{87,88} We will also use water as the reference for the susceptibility maps of this review.

In MRI, susceptibility has long been an enemy and a friend. It not only gives rise to artifacts^{89,90} (Figures 1b⁹¹ and c⁹⁰) but also serves as a cornerstone for advanced imaging techniques including functional MRI (fMRI),⁹² susceptibility weighted imaging (SWI)^{93,94} (Figure 1c⁹⁰) and quantitative susceptibility mapping (QSM)^{19,20,95,96} (Figure 1d⁹⁷). Susceptibility-induced artifacts, largely due to the susceptibility difference between air and water, are manifested by geometric distortions in echo-planar imaging (blue arrow in Figure 1b) and/or signal loss in SWI (red arrow in Figure 1c), particularly near the nasal cavity and ear canal, creating challenges in MRI. On the other hand, the temporal susceptibility change from the concentration variation in deoxygenated hemoglobin due to neurovascular coupling is the primary contrast mechanism for fMRI whereas the spatial susceptibility variation of tissue iron (e.g., ferritin and hemosiderin) and deoxygenated hemoglobin is the contrast source for SWI. In QSM, both paramagnetic sources (e.g., ferritin, hemosiderin and deoxy-hemoglobin) and diamagnetic sources (e.g., myelin and calcium) are responsible for the image contrast, delineating details of brain structures that may not be visible in conventional MRI methods.

Question 2: Susceptibility imaging is new to me. Can you give a brief introduction?

Answer 2: Sure. As I mentioned in Question and Answer 1, magnetic susceptibility serves as an important contrast source for MRI and there exist a few well-known susceptibility imaging methods such as SWI and QSM that provide important information of tissue microstructure and composition.

Susceptibility weighted imaging (SWI): One of the earliest methods in this field is SWI, which was originally named as venography.^{93,94} SWI is reconstructed using single- or multi-echo gradient echo (GRE) magnitude and phase images. The method enhances the visualization of tissues with different magnetic susceptibilities, making it particularly adept at highlighting veins, microbleeds, hemorrhages, and thrombosis where a high concentration of deoxy-hemoglobin exists⁹⁸ (green arrowheads in Figure 2a). Because microbleeds and hemorrhages are clinically important, the method has become a routine and invaluable protocol in many neuro exams.⁹⁹ Recently, an advanced susceptibility imaging method,

phase difference enhanced imaging,¹⁰⁰ has been proposed to enhance different tissues, visualizing fiber tracts such as optic radiation and enhancing the identification of differences in myelin density¹⁰¹.

Quantitative susceptibility mapping (QSM): Unlike traditional MRI, which primarily generates qualitative images, QSM provides quantitative information about the magnetic susceptibility of tissues, offering valuable insights into their microstructural composition.¹⁹ The method utilizes multi-echo GRE phase images to reconstruct quantitative susceptibility maps. Its ability to quantify tissue magnetic susceptibility provides a unique opportunity to differentiate between iron and calcium lesions, a capability derived from the inherent sign difference between diamagnetic calcium and paramagnetic iron, facilitating more accurate diagnoses.¹⁰² In MS, QSM has proven instrumental in categorizing lesions based on their iron and myelin concentration changes, offering insights into disease progression.^{103–106} Moreover, QSM plays a pivotal role in elucidating the accumulation of iron in deep gray matter structures, providing valuable information for various neurological disorders, including Parkinson's disease^{107,108} (Figure 2b) and Alzheimer's disease.^{109–111} These applications underscore QSM's potential to significantly impact the diagnosis, treatment planning, and understanding of diverse neurological conditions. An advanced QSM method, Susceptibility Tensor Imaging¹¹² extends the concept of QSM by considering the anisotropic nature of susceptibility in white matter due to its susceptibility anisotropy,¹¹³ creating fiber orientation information in white matter.

Susceptibility source separation: Recently, susceptibility imaging has witnessed significant advancements with the introduction of a susceptibility source separation method (χ -separation or chi-separation or x-separation),⁷³ a technique that holds great promise in disentangling the mixture of diamagnetic (or negative) sources and paramagnetic (or positive) sources within a voxel. Leveraging a biophysical model of the susceptibility induced magnetic field perturbation and R_2' ($= R_2^* - R_2 = 1/T_2^* - 1/T_2$), χ -separation allows for the differentiation of dia- and paramagnetic susceptibility sources, assuming a static dephasing regime with the same susceptibility characteristics for both sources (see Figure 3 for the details of the χ -separation model).^{73,75,76,84} This approach enables the creation of separate paramagnetic susceptibility maps and diamagnetic susceptibility maps (Figures 2c and d). In these maps, the definition of dia- and paramagnetic sources is referenced with respect to water. In the brain, where

iron constitutes a primary source of paramagnetism and myelin represents a significant diamagnetic source, this technique may deliver iron and myelin distributions of the brain, enabling researchers and clinicians to explore the intricacies of the brain and gain a more nuanced understanding of pathophysiological processes of diseases (see Question and Answer 9 for current and future applications). However, it is essential to note that χ -separation maps may exhibit inaccuracies stemming from various sources, such as the disruption of the static dephasing regime in regions with high susceptibility concentrations and differences in susceptibility characteristics between ferritin, the primary iron-protein in the brain, and myelin, which introduces susceptibility anisotropy (see Questions and Answers 3 and 5).

After χ -separation, more susceptibility source separation methods including DECOMPOSE,⁷⁴ χ -sepnet,¹¹⁴ R_2^* QSM^{77,78} and APART-QSM^{81,82}, have been developed to separate diamagnetic and paramagnetic sources within a voxel. While the original χ -separation utilizes multi-echo GRE images and multi-echo spin echo (SE) images for reconstruction,⁷³ more recent methods leverage R_2^* instead of R_2' , enhancing usability (i.e., R_2 map not required):^{74,77,114} For example, Chen et al.⁷⁴ utilized a different biophysical model that describes a direct relationship between R_2^* and susceptibility sources. In the work of Dimov et al., a linear relationship between R_2' and R_2^* is assumed^{77,78}, utilizing a linearly scaled R_2^* map as the input for χ -separation, removing the need for an R_2 map. For the similar purpose, a neural network, χ -sepnet- R_2^* ,¹¹⁴ is trained to directly reconstruct χ -separation maps from R_2^* and local field inputs.

Question 3: Can you tell me more about the diamagnetic susceptibility map generated from the susceptibility source separation technique?

Answer 3: In the brain, the main diamagnetic susceptibility source is myelin, while other sources, including calcium and some proteins, also exist. Calcium tends to concentrate in focal locations, making it easily distinguishable from myelin. Proteins exhibit varying susceptibilities; for example, oxy-hemoglobin is slightly diamagnetic, while deoxy-hemoglobin is paramagnetic. However, most proteins, excluding those containing metallic ions like ferritin, generally have susceptibilities close to water. Therefore, myelin stands out as the primary source of the diamagnetic susceptibility map both in gray

and white matter. By the way, the major paramagnetic susceptibility source is iron in the form of deoxy-hemoglobin, ferritin, and hemosiderin, with some rare diseases introducing additional sources such as copper in Wilson's disease.¹¹⁵

Unfortunately, myelin poses unique challenges due to its intricate structure and its complex nature in terms of susceptibility. Myelin exhibits susceptibility anisotropy, meaning its susceptibility measurement varies based on the orientation of the lipid bilayer to B_0 or, for myelinated axonal fibers, the fiber orientation to B_0 .^{112,113} Additionally, its multi-compartment microstructure (e.g., axonal space, myelin sheath, and extracellular space) creates a microstructure-induced field perturbation that is also orientation dependent.¹¹⁶⁻¹¹⁹ Moreover, not only field perturbation but also R_2^* , and consequently R_2' , are known to be fiber orientation dependent relative to B_0 .^{120,121}

These characteristics of myelin are not fully accounted for in the current models of susceptibility source separation, assuming the same susceptibility characteristics for both para- and diamagnetic susceptibility sources. As a result, susceptibility maps may contain errors in the quantification of myelin (and iron) concentration. While the effects of the orientation dependence require further investigation, they are anticipated to be relatively small compared to isotropic susceptibility (magnetic susceptibility anisotropy = 0.010 ppm vs. mean magnetic susceptibility = -0.042 ppm reported in reference¹²²). Thus, the errors from the orientation effects are expected to be limited, and the diamagnetic map from χ -separation effectively reflects myelin distribution in the brain (Figure 4). We must re-emphasize that the diamagnetic susceptibility map is a biomarker of myelin that indirectly reports myelin concentration. It should not be equated to a myelin susceptibility map nor a myelin density map.

Aside from the complex issue of myelin, diamagnetic susceptibility maps still contain non-myelin sources (see Question and Answer 5). Therefore, researchers should be careful in interpreting the maps.

Question 4: What is the evidence that the diamagnetic susceptibility map reflects myelin distribution?

Answer 4: Several findings suggest a strong association between the diamagnetic susceptibility map and myelin distribution. However, before delving into these findings, we want to emphasize that, just like other myelin imaging methods, the diamagnetic susceptibility map does not “equate” to a myelin

map (see Questions and Answers 3 and 5). Nevertheless, we believe it serves as a valuable surrogate biomarker for myelin, holding significant potential for various applications.

The first evidence that demonstrates the relationship between the diamagnetic susceptibility map and myelin distribution is the results from an ex-vivo brain specimen that includes the primary visual cortex (Figure 5⁷³). When the susceptibility map and myelin histology via Luxol fast blue (LFB) are compared, they show qualitatively similar distributions. For example, both images show a well-known cortical laminar structure in the primary visual cortex (yellow arrows: line of Gennari) and consistent contrasts among the three white matter fibers (red triangle: optic radiation, purple square: stratum sagittale internum, and green stars: forceps). When we reanalyzed the data for quantitative comparison, a high correlation ($R^2 = 0.770$; Figure 5d) was measured between the negative susceptibility values and LFB optical density values in the regions of interest (yellow circles and rectangles in Figure 5c), demonstrating that the diamagnetic susceptibility reports myelin concentration. When the cortex of the primary visual cortex (cyan region in Figure 5c) was segmented to generate a cortical profile, the results also confirm a strong consistency between the two profiles (Figure 5e), validating the technique for cortical myelin assessment. Both profiles successfully reveal the line of Gennari (green arrow in Figure 5e). These results suggest that we can generate a cortical profile of myelin using susceptibility source separation, opening the potential of exploring myelin concentration in the cortex as recently demonstrated in in-vivo human brain at 3T.³⁵

Another evidence from an ex-vivo specimen of the macaque brain can be found in the work by Li et al.,⁸¹ demonstrating a strong correlation between the diamagnetic susceptibility values and normalized myelin contents from LFB stained images among white matter fibers ($R^2 = 0.530$ in χ -separation and $R^2 = 0.854$ in APART-QSM).

In MS lesions, a study of R_2^* -QSM-based susceptibility source separation method demonstrated that the diamagnetic susceptibility maps of MS tissue samples report a reasonable correlation (correlation coefficient = 0.47, region of interest (ROI) analysis) with the optical density of myelin basic protein antibody stain.⁷⁸ This finding indicates that the map does show the connection to myelin even in pathological conditions, suggesting possibilities toward exploring brain pathologies using the technique.

Note that all of these validations are from ex-vivo samples, which do not contain vessels or other sources of artifacts observed in vivo. Hence, further complications may exist in in-vivo results.

For in-vivo maps, one can check the atlas of the diamagnetic susceptibility maps averaged over a large number of individuals.^{82,83} Overall, well-known fibers that connect long distances in the brain (e.g., corpus callosum, optic radiation, and internal capsule) reveal higher absolute contrast values ($|\chi_{\text{dia}}|$, Fig. 3 in reference⁸³). Of course, this contrast distribution can be observed in individual subjects as well (Figure 4). When the atlas is compared with that of MWI, they show pretty good correspondence, reporting a correlation of $R^2 = 0.63$ in the ROIs of white matter (Fig. 7 in reference⁸³). This result further corroborates that the diamagnetic susceptibility maps reflect myelin distribution in white matter although methodology-specific differences appear in the atlases (e.g., vessels and fiber orientation dependent contrast variations in the diamagnetic susceptibility atlas; overestimation of myelin water fraction in internal capsule in the MWI atlas).

Hence, both ex-vivo and in-vivo results confirm that the diamagnetic susceptibility is well-correlated with myelin distribution, suggesting that it can be used as an imaging biomarker for myelin.

Question 5: I can see non-myelin structures in the diamagnetic susceptibility map. What are they?

Answer 5: A diamagnetic susceptibility map reconstructed from a susceptibility source separation method may contain non-myelin structures that complicate direct interpretation of the map as a myelin distribution map. In the χ -separation maps, the most conspicuous source of artifacts is large vessels (see Figure 4, marked with red arrows). Flow inside the vessels induces signal variation and spatial displacement, resulting in inconsistent signal decay across echo time in the voxels inside and near the vessels. This inconsistency leads to incorrect R_2^* values, thus introducing errors in the resulting diamagnetic susceptibility values. Furthermore, the voxels inside the vessels violate the assumption of the static dephasing regime, further complicating the problem.

Another source of artifacts is non-local R_2^* effects due to large susceptibility differences at air-tissue interfaces and around large veins (Figure 4, marked with green arrows). It can induce overestimation of R_2^* values, producing errors in the diamagnetic susceptibility map. One may correct for the non-local R_2^* effects based on signal models.^{123,124}

Similar to QSM, streaking artifacts from imperfect dipole deconvolution are also a source of error. When using regularization-based algorithms (e.g., MEDI¹²⁵) for reconstruction, streaking artifacts may introduce erroneous estimation of myelin concentration. This can be mitigated by using multi-orientation data, as in the COSMOS¹²⁶ reconstruction in QSM, but is not practical because multiple scans are necessary, elongating the scan time. Reconstruction using a neural network trained with multi-orientation-reconstructed data (e.g., χ -sepnet¹¹⁴) can provide streaking artifact-free images (Figure 4) as demonstrated in QSM.⁹⁷

Question 6: How do I acquire data for susceptibility source separation?

Answer 6: The original χ -separation method involves acquiring 3D multi-echo GRE for the field and R_2^* maps and 2D multi-echo SE for the R_2 map. After the acquisition, the field and R_2' maps, where R_2' is calculated by $R_2^* - R_2$, are fed into the χ -separation algorithm.

For the multi-echo GRE protocol, you can use the recent recommendation outlined in the QSM consensus paper,¹²⁷ which suggests acquiring the whole brain in 6 min of scan time at the resolution of 1 mm isotropic voxel size with 5 echoes at 3T. For the SE protocol, multiple options exist; for example, a custom-designed 2D multi-echo SE with 6 echoes, an in-plane resolution of $1 \times 1 \text{ mm}^2$ and a slice thickness of 2 mm at the scan time of 12.4 min was used in the original χ -separation paper.⁷³ To shorten the scan time, a 2D dual echo Turbo SE product sequence can be employed, with parameters such as TR = 11000 ms, TE = 10 ms and 100 ms, in-plane resolution = $0.6 \times 0.6 \text{ mm}^2$ (required for clinical evaluation and later interpolated to 1 mm^2 for χ -separation), slice thickness = 2 mm, turbo factor = 7, acceleration factor = 2, and scan time = 7 min. In both cases, the thicker slice in the SE data needs to be interpolated to 1 mm to match the resolution of the GRE data. Advanced acquisition schemes have been explored for rapid simultaneous acquisition of GRE and SE data.^{79,128}

However, it is worth to note that all the SE acquisition methods or simultaneous acquisition approaches mentioned above may not be used in routine clinical scans or may not be available as a product sequence. This can result in substantially increased scan time, limiting the applicability of χ -separation. To overcome this challenge, alternative methods such as linear-scaling of R_2^* to R_2' ,^{77,78,82}

deep learning-powered R_2' generation,^{64,114} and a new model that only relies on multi-echo GRE data⁷⁴ have been proposed. While these methods improve the applicability, they may come with a trade-off of compromised accuracy. A few comparison results are underway,^{77,129} and further research is required to fully evaluate and compare different methods, particularly in clinical use cases.

Question 7: What about data processing? Any processing tools available for susceptibility source separation?

Answer 7: Yes, χ -separation toolbox is available (<https://github.com/SNU-LIST/chi-separation>), which includes the processing for the original χ -separation with the frequency and R_2' input, as well as deep learning-powered χ -separation using the frequency and R_2^* input or frequency and R_2' input. The toolbox incorporates all the pre-processing steps required for χ -separation, offering a comprehensive solution with multiple options, including denoising, for data processing. Other toolboxes are also accessible (<https://github.com/AMRI-Lab/APART-QSM>), providing alternatives for data analysis in susceptibility source separation techniques.

Here are additional details about data processing in susceptibility source separation, which requires generating local field and R_2' (or R_2^*) maps as the input to the source separation algorithm.

Local field: Local field perturbation from microstructural susceptibility sources is estimated similarly to QSM¹²⁷. Briefly, phase images from the multi-echo GRE data are unwrapped and echo combined (or echo-combined and then unwrapped). Subsequently a background field is removed to generate a local field perturbation map. We highly recommend readers to review the recent QSM consensus paper¹²⁷ to understand each step.

R_2 and R_2^* : An R_2' map is generated by the subtraction of R_2 from R_2^* . This process requires generation of R_2 and R_2^* maps from multi-echo SE and multi-echo GRE, respectively. While creating an R_2^* map can be straightforward by fitting an exponential decay function to the multi-echo magnitude data in each voxel, this map often becomes noisy and serves as a primary source of noise in χ -separation maps. Hence, denoising of the map via principal component analysis or deep learning may be useful.¹³⁰ Additionally, a few voxels may contain errors due to the background field or rapid loss of signal, requiring careful processing. Generating an R_2 map is more complicated due to the stimulated echoes in

multi-echo SE.¹³¹ This effect is well-known but can be a surprise for many people. It can be identified with the signature characteristics of the second echo reporting higher signal intensity than the first echo, necessitating correction methods for accurate R_2 estimation.¹³¹ Note that this issue does not happen in single echo SE and is largely mitigated in Turbo SE.

Susceptibility source separation algorithm: Once datasets are preprocessed, one can run a susceptibility source separation algorithm to generate para- and diamagnetic susceptibility maps. As mentioned in the previous section, several methods exist and we will explain χ -separation as an example. The algorithm estimates the para- and diamagnetic susceptibility concentrations by iteratively solving the minimization problem in Figure 3b. Similar to QSM, it requires solving the ill-conditioned dipole deconvolution problem, necessitating additional regularization such as MEDI¹²⁵ or iLSQR¹³², which are implemented in the toolbox. One may acquire multi-orientation dataset to convert the ill-conditioned problem to a well-conditioned one, generating a gold standard result. Alternatively, one can employ a neural network implementation of χ -sepnet- R_2' or χ -sepnet- R_2^* , which are trained on maps reconstructed using multi-orientation data.¹³³ Reconstruction using these networks significantly improves image quality. The χ -separation algorithm has been shown to select a long T_2 location (mostly CSF) as the reference with zero susceptibility,¹³⁴ differentiating it from QSM, which is required to set an explicit reference region (e.g., CSF or whole brain).

Question 8: I know there are other myelin imaging methods. What are pros and cons of the susceptibility source separation compared to them?

Answer 8: Several MRI techniques are available for visualizing myelin, either directly or indirectly. Comparing them is a complex task, and we recommend referring to the following review papers.²³⁻²⁸ In this section, we will briefly introduce well-known methods and then compare them against the susceptibility source separation technique.

MWI involves imaging water protons, known as myelin water, between the lipid bilayers of myelin. This myelin water exhibits a shorter relaxation time (T_2 , T_2^* , or T_1) than that of axonal or extracellular water, and this difference is exploited to generate MWI.¹⁻⁴ Another approach involves directly visualizing protons bound by the myelin lipid bilayers. These protons have limited mobility and are

strongly coupled, leading to a much shorter transverse relaxation time ($\ll 1$ ms) to be imaged using a conventional sequence. Studies have developed ultra-short echo time (UTE) imaging to address this challenge.^{15,17} Alternatively, magnetization transfer effects⁵ can be utilized to indirectly generate images from macromolecules. Several methods exist, including magnetization transfer ratio, magnetization transfer saturation, quantitative magnetization transfer,⁷ macromolecular proton fraction¹⁴ and inhomogeneous magnetization transfer.⁸ Myelin volume fraction from synthetic MRI^{10,11,135} also provides myelin information by relating the simultaneously measured T_1 , T_2 , and PD values to four partial volume components consisting of myelin, free water, cellular, and excess parenchymal partial volume components. Finally, quantitative R_1 imaging,^{12,16} R_2^* imaging,¹³⁶ and T_1 -weighted over T_2 -weighted imaging¹³ have also been proposed as indirect approaches to estimate myelin concentration in the brain.

All of these methods have their cons and pros. When comparing these methods, the susceptibility source separation technique with R_2^* -only (using only GRE data) has two clear advantages: acquisition in high resolution and application in ultra-high field MRI. As demonstrated in Figure 4, we can generate a 0.75 mm isotropic resolution map even at 3T in less than 6 min of scan time. At an ultra-high field strength, the technique benefits from both increased signal and increased susceptibility effects, creating a high-quality map at the resolution of 0.6 mm at 7T.¹³⁷ This advantage can be further extended to the susceptibility source separation method using R_2' when advanced acquisition schemes that allow simultaneous and rapid acquisition of GRE and SE data are applied.⁷⁹ On the other hand, MWI and UTE imaging suffer from a low signal-to-noise ratio, limiting their resolution. The synthetic MRI approach is limited by spatial resolution. Magnetization transfer requires a high specific absorption rate, which can restrict its application in ultra-high fields. Other methods (R_1 , R_2^* , T_1 -weighted over T_2 -weighted) are unable to remove contributions of iron, providing limited specificity (e.g., see Fig. 4 in reference³⁵). When it comes to the disadvantage of the susceptibility source separation, it shares the well-known challenge of GRE acquisition including sensitivity to spatial and temporal B_0 field inhomogeneity. In contrast, myelin imaging methods such as SE-based MWI,¹ UTE,^{15,17} and myelin volume fraction from synthetic MRI¹¹ are relatively robust to B_0 field inhomogeneity. Additionally, all the non-myelin

structures addressed in Question and Answer 5 may complicate the direct interpretation of the map as myelin.

Question 9: Applications so far and for the future?

Answer 9: Susceptibility source separation methods have found valuable applications in various neuroimaging studies, holding significant implications for both current clinical practices and future research endeavors. In MS studies, these techniques have proven instrumental in identifying lesions (Figure 6), particularly in cases with decreased iron and decreased myelin concentrations that may go unnoticed in conventional QSM (lesion 2 in Figure 6). These changes often lead to minimal alteration in QSM values, rendering these lesions potentially unidentified by QSM alone. However, susceptibility source separation provides sensitivity for detecting such lesions. Additionally, these methods showcase potential in comparing lesion characteristics between MS and Neuromyelitis Optica (NMO), offering a new avenue for differentiating these two diseases based on their lesion features.⁶⁴ The applications of susceptibility source separation are poised to extend to diagnosis, disease progression monitoring, and treatment efficacy assessment, with a notable potential to report on remyelination processes within lesions.

Beyond well-known demyelination diseases, susceptibility source separation methods may demonstrate broader applications. In neurodegenerative disorders such as Alzheimer's disease and Parkinson's disease, these techniques can facilitate the visualization of myelin and iron changes, providing insights into the structural alterations associated with these conditions.⁸⁰ The methodology may extend its reach to psychiatric disorders, including schizophrenia, bipolar disorder, and depression, where ongoing research explores the role of myelin.¹³⁸ Additionally, in the identification of seizure locations or in evaluating traumatic brain injury, the method may prove useful.^{139,140} Furthermore, susceptibility source separation can be applied in neuroscience, exploring developmental and aging brains. The study of myeloarchitecture can provide valuable insights into brain parcellation.³⁵ The current and potential applications of susceptibility source separation underscore its transformative potential in advancing our understanding of neurological and psychiatric conditions, as well as its contributions to neuroscience.

Conclusion

In conclusion, this review has traversed the exciting landscape of the rapidly growing area of the magnetic susceptibility source separation technique as a promising biomarker for myelin. As we stand at the forefront of this burgeoning field, we anticipate continued technical development, further validation, and the exploration of new applications, particularly capitalizing on its powerful advantage in high-resolution imaging at high-field MRI. It is also important to recognize that this technique extends beyond myelin, providing iron distribution, thus offering a complementary dimension to our understanding of the brain. However, it remains imperative to acknowledge that, like any method, magnetic susceptibility source separation has its limitations. A negative susceptibility map, while informative, does not equate to myelin content, emphasizing the importance of careful interpretation, particularly in pathological conditions. We strongly recommend that investigators intending to apply this technique understand the details of the technology, and we hope this review serves as a guiding step in that direction. Simultaneously, developers are encouraged to invest efforts in refining methods that allow for the direct interpretation of biological information, further propelling the potential of magnetic susceptibility source separation in advancing our understanding of the brain.

Acknowledgment

This work was supported by the National Research Foundation of Korea (NRF-2021R1A2B5B03002783, NRF-2019M3C7A1031994), IITP-2023-RS-2023-00256081, INMC and IOER at Seoul National University, and the Hankuk University of Foreign Studies Research Fund.

Conflicts of Interest

The authors have no conflicts of interest to disclose.

References

1. Mackay A, Whittall K, Adler J, Li D, Paty D, Graeb D. In vivo visualization of myelin water in brain by magnetic resonance. *Magnet Reson Med* 1994; 31:673–677.
2. Du YP, Chu R, Hwang D, et al. Fast multislice mapping of the myelin water fraction using multicompartment analysis of T decay at 3T: A preliminary postmortem study. *Magn Reson Med* 2007; 58:865–870.
3. Deoni SCL, Rutt BK, Arun T, Pierpaoli C, Jones DK. Gleaning multicomponent T₁ and T₂ information from steady-state imaging data: 2D Relaxometry With Steady-State Imaging. *Magnet Reson Med* 2008; 60:1372–1387.
4. Oh S-H, Bilello M, Schindler M, Markowitz CE, Detre JA, Lee J. Direct visualization of short transverse relaxation time component (ViSTa). *NeuroImage* 2013; 83:485–492.
5. Wolff SD, Balaban RS. Magnetization transfer contrast (MTC) and tissue water proton relaxation in vivo. *Magn Reson Med* 1989; 10:135–144.
6. Henkelman RM, Huang X, Xiang Q, Stanisz GJ, Swanson SD, Bronskill MJ. Quantitative interpretation of magnetization transfer. *Magnet Reson Med* 1993; 29:759–766.
7. Sled JG, Pike GB. Quantitative imaging of magnetization transfer exchange and relaxation properties in vivo using MRI. *Magn Reson Med* 2001; 46:923–931.
8. Varma G, Duhamel G, Bazelaire C de, Alsop DC. Magnetization transfer from inhomogeneously broadened lines: A potential marker for myelin. *Magn Reson Med* 2015; 73:614–622.
9. Song S-K, Sun S-W, Ju W-K, Lin S-J, Cross AH, Neufeld AH. Diffusion tensor imaging detects and differentiates axon and myelin degeneration in mouse optic nerve after retinal ischemia. *NeuroImage* 2003; 20:1714–1722.
10. Fujita S, Hagiwara A, Hori M, et al. Three-dimensional high-resolution simultaneous quantitative mapping of the whole brain with 3D-QALAS: An accuracy and repeatability study. *Magn Reson Imaging* 2019
11. Warntjes M, Engström M, Tisell A, Lundberg P. Modeling the Presence of Myelin and Edema in the Brain Based on Multi-Parametric Quantitative MRI. *Front Neurol* 2016; 7:16.
12. Bock NA, Kocharyan A, Liu JV, Silva AC. Visualizing the entire cortical myelination pattern in marmosets with magnetic resonance imaging. *J Neurosci Methods* 2009; 185:15–22.
13. Glasser MF, Essen DCV. Mapping Human Cortical Areas In Vivo Based on Myelin Content as Revealed by T₁- and T₂-Weighted MRI. *J Neurosci* 2011; 31:11597–11616.
14. Yarnykh VL. Fast macromolecular proton fraction mapping from a single off-resonance magnetization transfer measurement. *Magn Reson Med* 2012; 68:166–178.
15. Wilhelm MJ, Ong HH, Wehrli SL, et al. Direct magnetic resonance detection of myelin and prospects for quantitative imaging of myelin density. *Proc Natl Acad Sci* 2012; 109:9605–9610.

16. Lutti A, Dick F, Sereno MI, Weiskopf N. Using high-resolution quantitative mapping of R1 as an index of cortical myelination. *NeuroImage* 2014; 93:176–188.
17. Du J, Ma G, Li S, et al. Ultrashort echo time (UTE) magnetic resonance imaging of the short T2 components in white matter of the brain using a clinical 3T scanner. *NeuroImage* 2014; 87:32–41.
18. Hagiwara A, Hori M, Kamagata K, et al. Myelin Measurement: Comparison Between Simultaneous Tissue Relaxometry, Magnetization Transfer Saturation Index, and T1w/T2w Ratio Methods. *Sci Rep-uk* 2018; 8:10554.
19. Rochefort L de, Brown R, Prince MR, Wang Y. Quantitative MR susceptibility mapping using piece-wise constant regularized inversion of the magnetic field. *Magn Reson Med* 2008; 60:1003–1009.
20. Shmueli K, Zwart JA de, Gelderen P van, Li T, Dodd SJ, Duyn JH. Magnetic susceptibility mapping of brain tissue in vivo using MRI phase data. *Magn Reson Med* 2009; 62:1510–1522.
21. Liu C, Li W, Johnson GA, Wu B. High-field (9.4T) MRI of brain dysmyelination by quantitative mapping of magnetic susceptibility. *NeuroImage* 2011; 56:930–938.
22. Lee J, Shmueli K, Kang B-T, et al. The contribution of myelin to magnetic susceptibility-weighted contrasts in high-field MRI of the brain. *NeuroImage* 2012; 59:3967–3975.
23. Laule C, Vavasour IM, Kolind SH, et al. Magnetic resonance imaging of myelin. *Neurotherapeutics* 2007; 4:460–484.
24. Alonso-Ortiz E, Levesque IR, Pike GB. MRI-based myelin water imaging: A technical review. *Magn Reson Med* 2015; 73:70–81.
25. Heath F, Hurley SA, Johansen-Berg H, Sampaio-Baptista C. Advances in noninvasive myelin imaging. *Dev Neurobiol* 2018; 78:136–151.
26. Lee J, Hyun J, Lee J, et al. So You Want to Image Myelin Using MRI: An Overview and Practical Guide for Myelin Water Imaging. *J Magn Reson Imaging* 2021; 53:360–373.
27. Piredda GF, Hilbert T, Thiran J, Kober T. Probing myelin content of the human brain with MRI: A review. *Magn Reson Med* 2021; 85:627–652.
28. Weijden CWJ van der, García DV, Borra RJH, et al. Myelin quantification with MRI: A systematic review of accuracy and reproducibility. *NeuroImage* 2021; 226:117561.
29. Clark VP, Courchesne E, Grafe M. In vivo Myeloarchitectonic Analysis of Human Striate and Extrastriate Cortex Using Magnetic Resonance Imaging. *Cereb Cortex* 1992; 2:417–424.
30. Watson JDG, Myers R, Frackowiak RSJ, et al. Area V5 of the Human Brain: Evidence from a Combined Study Using Positron Emission Tomography and Magnetic Resonance Imaging. *Cereb Cortex* 1993; 3:79–94.
31. Yoshiura T, Higano S, Rubio A, et al. Heschl and Superior Temporal Gyri: Low Signal Intensity of the Cortex on T2-weighted MR Images of the Normal Brain. *Radiology* 2000; 214:217–221.
32. Barbier EL, Marrett S, Danek A, et al. Imaging cortical anatomy by high-resolution MR at 3.0T: Detection of the stripe of Gennari in visual area 17. *Magn Reson Med* 2002; 48:735–738.

33. Martino FD, Moerel M, Xu J, et al. High-Resolution Mapping of Myeloarchitecture In Vivo: Localization of Auditory Areas in the Human Brain. *Cereb Cortex* 2015; 25:3394–3405.
34. Sereno MI, Lutti A, Weiskopf N, Dick F. Mapping the Human Cortical Surface by Combining Quantitative T1 with Retinotopy†. *Cereb Cortex* 2013; 23:2261–2268.
35. Lee S, Shin H-G, Kim M, Lee J. Depth-wise profiles of iron and myelin in the cortex and white matter using χ -separation: A preliminary study. *NeuroImage* 2023; 273:120058.
36. Hüppi PS, Maier SE, Peled S, et al. Microstructural Development of Human Newborn Cerebral White Matter Assessed in Vivo by Diffusion Tensor Magnetic Resonance Imaging. *Pediatr Res* 1998; 44:584–590.
37. Schmithorst VJ, Wilke M, Dardzinski BJ, Holland SK. Correlation of White Matter Diffusivity and Anisotropy with Age during Childhood and Adolescence: A Cross-sectional Diffusion-Tensor MR Imaging Study. *Radiology* 2002; 222:212–218.
38. Mabbott DJ, Noseworthy M, Bouffet E, Laughlin S, Rockel C. White matter growth as a mechanism of cognitive development in children. *NeuroImage* 2006; 33:936–946.
39. Whitaker KJ, Kolind SH, MacKay AL, Clark CM. Quantifying development: Investigating highly myelinated voxels in preadolescent corpus callosum. *NeuroImage* 2008; 43:731–735.
40. Deoni SCL, Mercure E, Blasi A, et al. Mapping Infant Brain Myelination with Magnetic Resonance Imaging. *J Neurosci* 2011; 31:784–791.
41. Deoni SCL, Dean DC, O’Muircheartaigh J, Dirks H, Jerskey BA. Investigating white matter development in infancy and early childhood using myelin water fraction and relaxation time mapping. *NeuroImage* 2012; 63:1038–1053.
42. O’Muircheartaigh J, Dean DC, Dirks H, et al. Interactions between White Matter Asymmetry and Language during Neurodevelopment. *J Neurosci* 2013; 33:16170–16177.
43. Dean DC, O’Muircheartaigh J, Dirks H, et al. Modeling healthy male white matter and myelin development: 3 through 60months of age. *NeuroImage* 2014; 84:742–752.
44. Lang DJM, Yip E, MacKay AL, et al. 48 echo T2 myelin imaging of white matter in first-episode schizophrenia: Evidence for aberrant myelination. *NeuroImage: Clin* 2014; 6:408–414.
45. Dean DC, O’Muircheartaigh J, Dirks H, et al. Characterizing longitudinal white matter development during early childhood. *Brain Struct Funct* 2015; 220:1921–1933.
46. Schmithorst VJ, Wilke M, Dardzinski BJ, Holland SK. Cognitive functions correlate with white matter architecture in a normal pediatric population: A diffusion tensor MRI study. *Hum Brain Mapp* 2005; 26:139–147.
47. Armstrong CL, Traipe E, Hunter JV, et al. Age-related, regional, hemispheric, and medial-lateral differences in myelin integrity in vivo in the normal adult brain. *AJNR Am J Neuroradiol* 2004; 25:977–84.
48. Sui YV, Masurkar AV, Rusinek H, Reisberg B, Lazar M. Cortical myelin profile variations in healthy aging brain: A T1w/T2w ratio study. *NeuroImage* 2022; 264:119743.

49. Pfefferbaum A, Sullivan EV, Hedehus M, Lim KO, Adalsteinsson E, Moseley M. Age-related decline in brain white matter anisotropy measured with spatially corrected echo-planar diffusion tensor imaging. *Magn Reson Med* 2000; 44:259–268.
50. Kirby ED, Frizzell TO, Grajauskas LA, et al. Increased myelination plays a central role in white matter neuroplasticity. *NeuroImage* 2022; 263:119644.
51. Lakhani B, Borich MR, Jackson JN, et al. Motor Skill Acquisition Promotes Human Brain Myelin Plasticity. *Neural Plast* 2016; 2016:7526135.
52. Dousset V, Grossman RI, Ramer KN, et al. Experimental allergic encephalomyelitis and multiple sclerosis: lesion characterization with magnetization transfer imaging. *Radiology* 1992; 182:483–491.
53. Henry RG, Oh J, Nelson SJ, Pelletier D. Directional diffusion in relapsing-remitting multiple sclerosis: A possible in vivo signature of Wallerian degeneration. *J Magn Reson Imaging* 2003; 18:420–426.
54. Laule C, Vavasour IM, Moore GRW, et al. Water content and myelin water fraction in multiple sclerosis. *J Neurol* 2004; 251:284–293.
55. Obberghen EV, Mchinda S, Troter A le, et al. Evaluation of the Sensitivity of Inhomogeneous Magnetization Transfer (ihMT) MRI for Multiple Sclerosis. *Am J Neuroradiol* 2018; 39:634–641.
56. Zhang L, Wen B, Chen T, et al. A comparison study of inhomogeneous magnetization transfer (ihMT) and magnetization transfer (MT) in multiple sclerosis based on whole brain acquisition at 3.0 T. *Magn Reson Imaging* 2020; 70:43–49.
57. Gass A, Barker GJ, Kidd D, et al. Correlation of magnetization transfer ratio with clinical disability in multiple sclerosis. *Ann Neurol* 1994; 36:62–67.
58. Martin P, Hagberg GE, Schultz T, et al. T2-Pseudonormalization and Microstructural Characterization in Advanced Stages of Late-infantile Metachromatic Leukodystrophy. *Clin Neuroradiol* 2021; 31:969–980.
59. Mangeat G, Ouellette R, Wabartha M, et al. Machine Learning and Multiparametric Brain MRI to Differentiate Hereditary Diffuse Leukodystrophy with Spheroids from Multiple Sclerosis. *J Neuroimaging* 2020; 30:674–682.
60. Steenweg ME, Wolf NI, Wieringen WN van, Barkhof F, Knaap MS van der, Pouwels PJW. Quantitative MRI in hypomyelinating disorders. *Neurology* 2016; 87:752–758.
61. Dreha-Kulaczewski SF, Brockmann K, Henneke M, et al. Assessment of myelination in hypomyelinating disorders by quantitative MRI. *J Magn Reson Imaging* 2012; 36:1329–1338.
62. Jeong IH, Choi JY, Kim S-H, et al. Comparison of myelin water fraction values in periventricular white matter lesions between multiple sclerosis and neuromyelitis optica spectrum disorder. *Mult Scler J* 2016; 22:1616–1620.
63. Manogaran P, Vavasour I, Borich M, et al. Corticospinal tract integrity measured using transcranial magnetic stimulation and magnetic resonance imaging in neuromyelitis optica and multiple sclerosis. *Mult Scler J* 2015; 22:43–50.

64. Kim W, Shin H-G, Lee H, et al. χ -Separation Imaging for Diagnosis of Multiple Sclerosis versus Neuromyelitis Optica Spectrum Disorder. *Radiology* 2022; 307:e220941.
65. Loevner LA, Grossman RI, Cohen JA, Lexa FJ, Kessler D, Kolson DL. Microscopic disease in normal-appearing white matter on conventional MR images in patients with multiple sclerosis: assessment with magnetization-transfer measurements. *Radiology* 1995; 196:511–515.
66. Faizy TD, Thaler C, Kumar D, et al. Heterogeneity of Multiple Sclerosis Lesions in Multislice Myelin Water Imaging. *PLoS ONE* 2016; 11:e0151496.
67. Choi JY, Jeong IH, Oh S, et al. Evaluation of Normal-Appearing White Matter in Multiple Sclerosis Using Direct Visualization of Short Transverse Relaxation Time Component (ViSTa) Myelin Water Imaging and Gradient Echo and Spin Echo (GRASE) Myelin Water Imaging. *J Magn Reson Imaging* 2019; 49:1091–1098.
68. Jeong IH, Choi JY, Kim S -H., et al. Normal-appearing white matter demyelination in neuromyelitis optica spectrum disorder. *Eur J Neurol* 2017; 24:652–658.
69. Vavasour IM, Laule C, Li DKB, et al. Longitudinal changes in myelin water fraction in two MS patients with active disease. *J Neurol Sci* 2009; 276:49–53.
70. Levesque IR, Giacomini PS, Narayanan S, et al. Quantitative magnetization transfer and myelin water imaging of the evolution of acute multiple sclerosis lesions. *Magn Reson Med* 2010; 63:633–640.
71. Zhu Z, Naji N, Esfahani JH, et al. MR Susceptibility Separation for Quantifying Lesion Paramagnetic and Diamagnetic Evolution in Relapsing–Remitting Multiple Sclerosis. *J Magn Reson Imaging* 2024
72. Tanikawa M, Nakahara J, Hata J, et al. q-Space Myelin Map imaging for longitudinal analysis of demyelination and remyelination in multiple sclerosis patients treated with fingolimod: A preliminary study. *J Neurol Sci* 2017; 373:352–357.
73. Shin H-G, Lee J, Yun YH, et al. χ -separation: Magnetic susceptibility source separation toward iron and myelin mapping in the brain. *NeuroImage* 2021; 240:118371.
74. Chen J, Gong N-J, Chaim KT, Otaduy MCG, Liu C. Decompose quantitative susceptibility mapping (QSM) to sub-voxel diamagnetic and paramagnetic components based on gradient-echo MRI data. *NeuroImage* 2021; 242:118477.
75. Emmerich J, Bachert P, Ladd ME, Straub S. A novel phantom with dia- and paramagnetic substructure for quantitative susceptibility mapping and relaxometry. *Phys Med* 2021; 88:278–284.
76. Emmerich J, Bachert P, Ladd ME, Straub S. On the separation of susceptibility sources in quantitative susceptibility mapping: Theory and phantom validation with an in vivo application to multiple sclerosis lesions of different age. *J Magn Reson* 2021; 330:107033.
77. Dimov AV, Nguyen TD, Gillen KM, et al. Susceptibility source separation from gradient echo data using magnitude decay modeling. *J Neuroimaging* 2022; 32:852–859.
78. Dimov AV, Gillen KM, Nguyen TD, et al. Magnetic Susceptibility Source Separation Solely from Gradient Echo Data: Histological Validation. *Tomography* 2022; 8:1544–1551.

79. Zhang Z, Cho J, Wang L, et al. Blip up-down acquisition for spin- and gradient-echo imaging (BUDA-SAGE) with self-supervised denoising enables efficient T2, T2*, para- and dia-magnetic susceptibility mapping. *Magn Reson Med* 2022; 88:633–650.
80. Ahmed M, Chen J, Arani A, et al. The diamagnetic component map from quantitative susceptibility mapping (QSM) source separation reveals pathological alteration in Alzheimer's disease-driven neurodegeneration. *NeuroImage* 2023; 280:120357.
81. Li Z, Feng R, Liu Q, et al. APART-QSM: An improved sub-voxel quantitative susceptibility mapping for susceptibility source separation using an iterative data fitting method. *NeuroImage* 2023; 274:120148.
82. Lao G, Liu Q, Li Z, et al. Sub-voxel quantitative susceptibility mapping for assessing whole-brain magnetic susceptibility from ages 4 to 80. *Hum Brain Mapp* 2023:5953–5971.
83. Min K, Sohn B, Kim WJ, et al. A human brain atlas of chi-separation for normative iron and myelin distributions. *arXiv* 2023
84. Straub S, El-Sanousy E, Emmerich J, Sandig FL, Ladd ME, Schlemmer H. Quantitative magnetic resonance imaging biomarkers for cortical pathology in multiple sclerosis at 7 T. *NMR Biomed* 2023; 36:e4847.
85. Schenck JF. The role of magnetic susceptibility in magnetic resonance imaging: MRI magnetic compatibility of the first and second kinds. *Med Phys* 1996; 23:815–850.
86. Weast RC, Astle MJ. *CRC Handbook of Chemistry and Physics*. 1981
87. Liu Z, Spincemaille P, Yao Y, Zhang Y, Wang Y. MEDI+0: Morphology enabled dipole inversion with automatic uniform cerebrospinal fluid zero reference for quantitative susceptibility mapping. *Magn Reson Med* 2018; 79:2795–2803.
88. Dimov AV, Nguyen TD, Spincemaille P, et al. Global cerebrospinal fluid as a zero-reference regularization for brain quantitative susceptibility mapping. *J Neuroimaging* 2022; 32:141–147.
89. Jezzard P, Balaban RS. Correction for geometric distortion in echo planar images from B0 field variations. *Magn Reson Med* 1995; 34:65–73.
90. Oh SS, Oh S, Nam Y, et al. Improved susceptibility weighted imaging method using multi-echo acquisition. *Magn Reson Med* 2014; 72:452–458.
91. Oh S, Chung J, In M, et al. Distortion correction in EPI at ultra-high-field MRI using PSF mapping with optimal combination of shift detection dimension. *Magn Reson Med* 2012; 68:1239–1246.
92. Ogawa S, Tank DW, Menon R, et al. Intrinsic signal changes accompanying sensory stimulation: functional brain mapping with magnetic resonance imaging. *Proc Natl Acad Sci* 1992; 89:5951–5955.
93. Reichenbach JR, Venkatesan R, Schillinger DJ, Kido DK, Haacke EM. Small vessels in the human brain: MR venography with deoxyhemoglobin as an intrinsic contrast agent. *Radiology* 1997; 204:272–277.
94. Haacke EM, Xu Y, Cheng YN, Reichenbach JR. Susceptibility weighted imaging (SWI). *Magn Reson Med* 2004; 52:612–618.

95. Committee QCO, Bilgic B, Costagli M, et al. Recommended implementation of quantitative susceptibility mapping for clinical research in the brain: A consensus of the ISMRM electro-magnetic tissue properties study group. *Magn Reson Med* 2024
96. Wang Y, Liu T. Quantitative susceptibility mapping (QSM): Decoding MRI data for a tissue magnetic biomarker. *Magn Reson Med* 2015; 73:82–101.
97. Yoon J, Gong E, Chatnuntawech I, et al. Quantitative susceptibility mapping using deep neural network: QSMnet. *NeuroImage* 2018; 179:199–206.
98. Tong KA, Ashwal S, Holshouser BA, et al. Hemorrhagic Shearing Lesions in Children and Adolescents with Posttraumatic Diffuse Axonal Injury: Improved Detection and Initial Results. *Radiology* 2003; 227:332–339.
99. Haller S, Haacke EM, Thurnher MM, Barkhof F. Susceptibility-weighted Imaging: Technical Essentials and Clinical Neurologic Applications. *Radiology* 2021; 299:3–26.
100. Kakeda S, Korogi Y, Yoneda T, et al. A novel tract imaging technique of the brainstem using phase difference enhanced imaging: normal anatomy and initial experience in multiple system atrophy. *Eur Radiol* 2011; 21:2202.
101. Tatewaki Y, Mutoh T, Thyreau B, et al. Phase Difference-Enhanced Magnetic Resonance (MR) Imaging (PADRE) Technique for the Detection of Age-Related Microstructural Changes in Optic Radiation: Comparison with Diffusion Tensor Imaging (DTI). *Méd Sci Monit : Int Méd J Exp Clin Res* 2017; 23:5495–5503.
102. Chen W, Zhu W, Kovanlikaya Ii, et al. Intracranial Calcifications and Hemorrhages: Characterization with Quantitative Susceptibility Mapping. *Radiology* 2014; 270:496–505.
103. Langkammer C, Liu T, Khalil M, et al. Quantitative Susceptibility Mapping in Multiple Sclerosis. *Radiology* 2013; 267:551–559.
104. Walsh AJ, Blevins G, Lebel RM, Seres P, Emery DJ, Wilman AH. Longitudinal MR Imaging of Iron in Multiple Sclerosis: An Imaging Marker of Disease. *Radiology* 2013; 270:186–196.
105. Eskreis-Winkler S, Deh K, Gupta A, et al. Multiple sclerosis lesion geometry in quantitative susceptibility mapping (QSM) and phase imaging. *J Magn Reson Imaging* 2015; 42:224–229.
106. Wisnieff C, Ramanan S, Olesik J, Gauthier S, Wang Y, Pitt D. Quantitative susceptibility mapping (QSM) of white matter multiple sclerosis lesions: Interpreting positive susceptibility and the presence of iron. *Magn Reson Med* 2015; 74:564–570.
107. Langkammer C, Pirpamer L, Seiler S, et al. Quantitative Susceptibility Mapping in Parkinson's Disease. *PLoS ONE* 2016; 11:e0162460.
108. Kim EY, Sung YH, Shin H-G, Noh Y, Nam Y, Lee J. Diagnosis of Early-Stage Idiopathic Parkinson's Disease Using High-Resolution Quantitative Susceptibility Mapping Combined with Histogram Analysis in the Substantia Nigra at 3 T. *J Clin Neurol* 2018; 14:90–97.
109. Acosta-Cabronero J, Williams GB, Cardenas-Blanco A, Arnold RJ, Lupson V, Nestor PJ. In Vivo Quantitative Susceptibility Mapping (QSM) in Alzheimer's Disease. *PLoS ONE* 2013; 8:e81093.

110. Moon Y, Han S-H, Moon W-J. Patterns of Brain Iron Accumulation in Vascular Dementia and Alzheimer's Dementia Using Quantitative Susceptibility Mapping Imaging. *J Alzheimer's Dis* 2016; 51:737–745.
111. Kim HW, Lee S, Yang JH, Moon Y, Lee J, Moon W-J. Cortical Iron Accumulation as an Imaging Marker for Neurodegeneration in Clinical Cognitive Impairment Spectrum: A Quantitative Susceptibility Mapping Study. *Korean J Radiol* 2023; 24:1131–1141.
112. Liu C. Susceptibility tensor imaging. *Magn Reson Med* 2010; 63:1471–1477.
113. Lee J, Shmueli K, Fukunaga M, et al. Sensitivity of MRI resonance frequency to the orientation of brain tissue microstructure. *Proc Natl Acad Sci* 2010; 107:5130–5135.
114. Kim M, Shin H-G, Oh C, et al. Chi-sepnet: Susceptibility source separation using deep neural network. *Proceedings of the 30th Annual ISMRM Meeting, London, 2022*; 2464
115. Fritzsche D, Reiss-Zimmermann M, Trampel R, Turner R, Hoffmann K-T, Schäfer A. Seven-Tesla Magnetic Resonance Imaging in Wilson Disease Using Quantitative Susceptibility Mapping for Measurement of Copper Accumulation. *Investig Radiol* 2014; 49:299–306.
116. Wharton S, Bowtell R. Fiber orientation-dependent white matter contrast in gradient echo MRI. *Proc Natl Acad Sci* 2012; 109:18559–18564.
117. Sati P, Gelderen P van, Silva AC, et al. Micro-compartment specific T2* relaxation in the brain. *NeuroImage* 2013; 77:268–278.
118. Wharton S, Bowtell R. Effects of white matter microstructure on phase and susceptibility maps. *Magn Reson Med* 2015; 73:1258–1269.
119. Lee J, Nam Y, Choi JY, Kim EY, Oh S, Kim D. Mechanisms of T2* anisotropy and gradient echo myelin water imaging. *NMR Biomed* 2017; 30:e3513.
120. Denk C, Torres EH, MacKay A, Rauscher A. The influence of white matter fibre orientation on MR signal phase and decay. *NMR Biomed* 2011; 24:246–252.
121. Lee J, Gelderen P van, Kuo L-W, Merkle H, Silva AC, Duyn JH. T2*-based fiber orientation mapping. *NeuroImage* 2011; 57:225–234.
122. Li X, Vikram DS, Lim IAL, Jones CK, Farrell JAD, Zijl PCM van. Mapping magnetic susceptibility anisotropies of white matter in vivo in the human brain at 7T. *NeuroImage* 2012; 62:314–330.
123. Yablonskiy DA, Sukstanskii AL, Luo J, Wang X. Voxel spread function method for correction of magnetic field inhomogeneity effects in quantitative gradient-echo-based MRI. *Magn Reson Med* 2013; 70:1283–1292.
124. Lee D, Lee J, Lee J, Nam Y. Single-scan z-shim method for reducing susceptibility artifacts in gradient echo myelin water imaging. *Magn Reson Med* 2018; 80:1101–1109.
125. Liu T, Liu J, Rochefort L de, et al. Morphology enabled dipole inversion (MEDI) from a single-angle acquisition: Comparison with COSMOS in human brain imaging. *Magn Reson Med* 2011; 66:777–783.

126. Liu T, Spincemaille P, Rochefort L de, Kressler B, Wang Y. Calculation of susceptibility through multiple orientation sampling (COSMOS): A method for conditioning the inverse problem from measured magnetic field map to susceptibility source image in MRI. *Magn Reson Med* 2009; 61:196–204.
127. Bilgic B, Costagli M, Chan K-S, et al. Recommended Implementation of Quantitative Susceptibility Mapping for Clinical Research in The Brain: A Consensus of the ISMRM Electro-Magnetic Tissue Properties Study Group. *arXiv* 2023
128. Ji S, Yang D, Lee J, Choi SH, Kim H, Kang KM. Synthetic MRI: Technologies and Applications in Neuroradiology. *J Magn Reson Imaging* 2020:1013–1025.
129. Shin H-G, Chen J, Lee J, et al. QALAS + QSM: Efficient Multi-parameter Mapping Allows Disentangling Para- and Dia-magnetic Contributions in Brain Tissue. *Proceedings of the 30th Annual ISMRM Meeting, London, 2022; 2465*
130. Song JE, Kim D-H. Improved Multi-Echo Gradient-Echo-Based Myelin Water Fraction Mapping Using Dimensionality Reduction. *IEEE Trans Méd Imaging* 2022; 41:27–38.
131. Lebel RM, Wilman AH. Transverse relaxometry with stimulated echo compensation. *Magnet Reson Med* 2010; 64:1005–1014.
132. Li W, Wang N, Yu F, et al. A method for estimating and removing streaking artifacts in quantitative susceptibility mapping. *NeuroImage* 2015; 108:111–122.
133. Shin H-G, Seo J, Lee Y, et al. chi-separation using multi-orientation data in *invivo* and *exvivo* brains: Visualization of histology up to the resolution of 350 μm . *Proceedings of the 30th Annual ISMRM Meeting, London, 2022; 0771*
134. Lee J, Hwang T, Nam Y, Oh S-H, Lee and J. An automatically referenced quantitative susceptibility mapping algorithm: QSMauto_ref. *Proceedings of the 26th Annual ISMRM Meeting, 2018; 2206*
135. Hagiwara A, Hori M, Yokoyama K, et al. Utility of a Multiparametric Quantitative MRI Model That Assesses Myelin and Edema for Evaluating Plaques, Periplaque White Matter, and Normal-Appearing White Matter in Patients with Multiple Sclerosis: A Feasibility Study. *Am J Neuroradiol* 2017; 38:237–242.
136. Cohen-Adad J, Polimeni JR, Helmer KG, et al. T2* mapping and B0 orientation-dependence at 7T reveal cyto- and myeloarchitecture organization of the human cortex. *NeuroImage* 2012; 60:1006–1014.
137. Ji S, Park J, Shin H-G, Kim M, Lee and J. In-vivo delineation of fine structures in the human brain using high resolution deep learning-powered chi-separation. *Proceedings of the 31st Annual ISMRM Meeting, Toronto, 2023; 1045*
138. Nave K-A, Ehrenreich H. Myelination and Oligodendrocyte Functions in Psychiatric Diseases. *JAMA Psychiatry* 2014; 71:582–584.
139. Weber AM, Torres C, Rauscher A. Imaging the Role of Myelin in Concussion. *Neuroimaging Clin North Am* 2018; 28:83–90.

140. Choi JY, Hart T, Whyte J, et al. Myelin water imaging of moderate to severe diffuse traumatic brain injury. *NeuroImage: Clin* 2019; 22:101785.

Figures

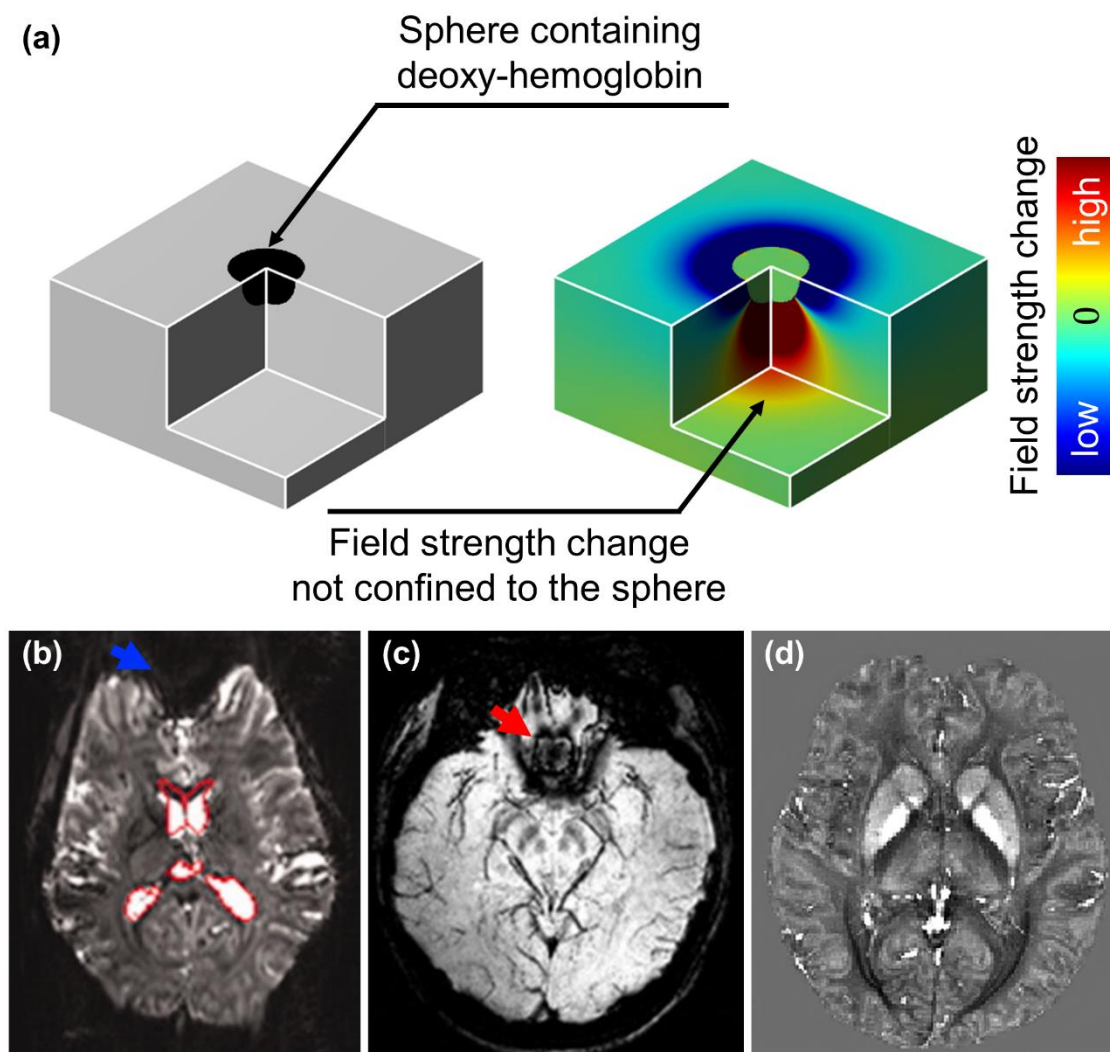


Figure 1. (a) A demonstration of field perturbation from a paramagnetic sphere in MRI. The sphere is assumed to contain a large number of deoxygenated hemoglobin proteins as the susceptibility source (left) and they create B₀ field perturbation in and outside of the sphere (right). (b) Susceptibility-induced geometric distortion (blue arrow) in an echo-planar image due to the susceptibility difference between air-tissue interfaces. Copyright 2011 Wiley. Adapted and used with permission from Se-Hong Oh, Jun-Young Chung, Myung-Ho In, Maxim Zaitsev, Young-Bo Kim, Oliver Speck, Zang-Hee Cho, *Distortion correction in EPI at ultra-high-field MRI using PSF mapping with optimal combination of shift detection dimension*, *Magnetic Resonance in Medicine*, Wiley. (c) An SWI image and its artifact (red arrow). Copyright 2014 Wiley. Adapted and used with permission from Sung Suk Oh, Se-Hong Oh, Yoonho Nam, Dongyeob Han, Randall B. Stafford, Jinyoung Hwang, Dong-Hyun Kim, HyunWook Park, Jongho Lee,

Improved susceptibility weighted imaging method using multi-echo acquisition, Magnetic Resonance in Medicine, Wiley. (d) A QSM image. Adapted and reprinted from Neuroimage, 179, Jaeyeon Yoon, Enhao Gong, Itthi Chatnuntaweck, Berkin Bilgic, Jingu Lee, Woojin Jung, Jingyu Ko, Hosan Jung, Kawin Setsompop, Greg Zaharchuk, Eung Yeop Kim, John Pauly, Jongho Lee, Quantitative susceptibility mapping using deep neural network: QSMnet, 119-206, Copyright 2018, with permission from Elsevier.

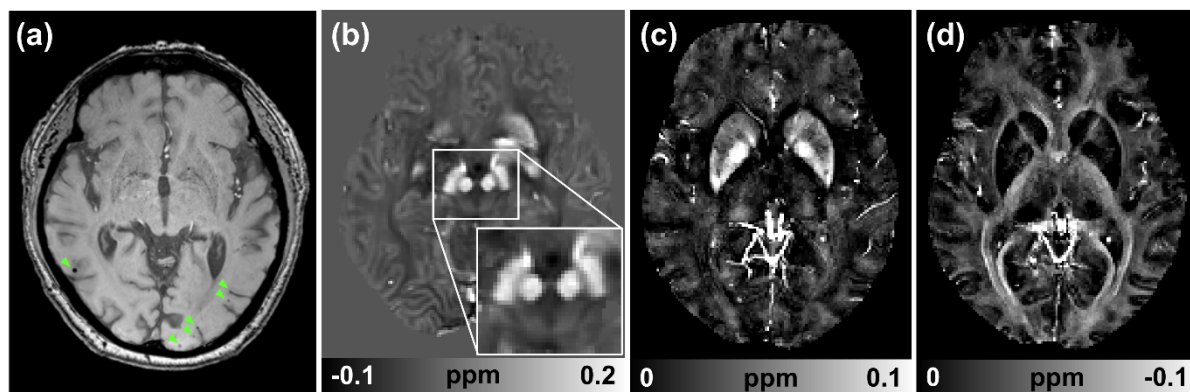
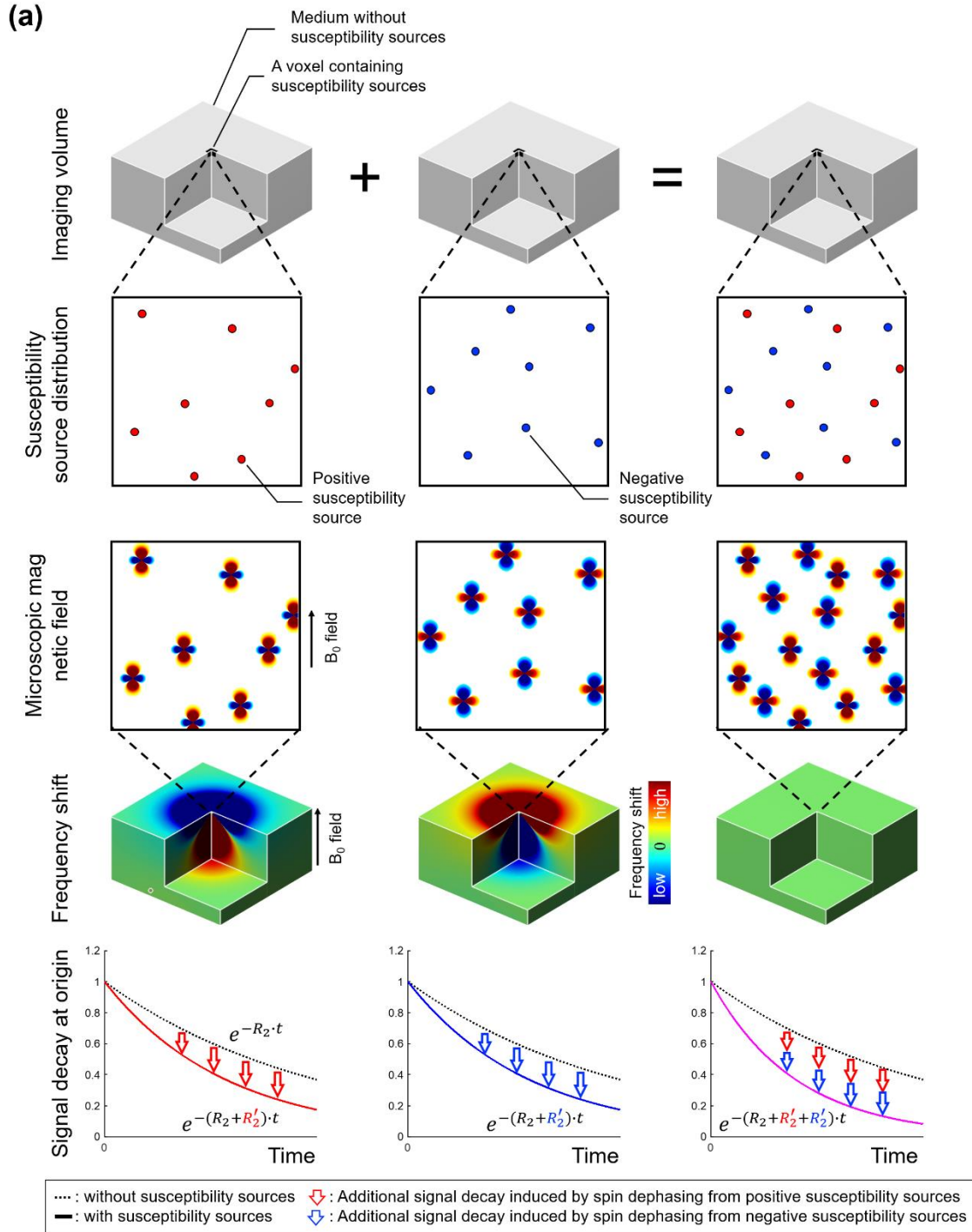


Figure 2. (a) An SWI image with small hemorrhagic lesions (green arrowheads), (b) A QSM map from a Parkinson's disease patient, (c) a χ -separation paramagnetic susceptibility map and (d) a diamagnetic susceptibility map. (c,d) are adapted from NeuroImage, 240, Shin Hyeong-Geol, Lee Jingu, Yun Young Hyun, Yoo Seong Ho, Jang Jinhee, Oh Se-Hong, Nam Yoonho, Jung Sehoon, Kim Sunhye, Masaki Fukunaga, Kim Woojun, Choi Hyung Jin, Lee Jongho, χ -separation: Magnetic susceptibility source separation toward iron and myelin mapping in the brain, 118371, Copyright 2021, with permission from Elsevier.



(b)

Frequency domain equation:

$$\Delta f(\mathbf{r}) = D_f(\mathbf{r}) * (\chi_{para}(\mathbf{r}) + \chi_{dia}(\mathbf{r}))$$

Magnitude domain equation:

$$R_2'(\mathbf{r}) = D_{r,para}(\mathbf{r}) \cdot |\chi_{para}(\mathbf{r})| + D_{r,dia}(\mathbf{r}) \cdot |\chi_{dia}(\mathbf{r})|$$

Combined model for χ -separation:

$$\underset{\chi_{para}, \chi_{dia}}{\operatorname{argmin}} \left\{ |R_2'(\mathbf{r}) + i2\pi\Delta f(\mathbf{r}) - D_r \cdot (|\chi_{para}(\mathbf{r})| + |\chi_{dia}(\mathbf{r})|) - i2\pi D_f(\mathbf{r}) * (\chi_{para}(\mathbf{r}) + \chi_{dia}(\mathbf{r}))| + \lambda \cdot \underset{\text{optional regularization}}{g(\chi_{para}(\mathbf{r}), \chi_{dia}(\mathbf{r}))} \right\}$$

Figure 3. Contrast mechanism of χ -separation. **(a)** The effects of paramagnetic and diamagnetic susceptibility on frequency and magnitude of MR images. *Adapted and reprinted from NeuroImage, 240, Shin Hyeong-Geol, Lee Jingu, Yun Young Hyun, Yoo Seong Ho, Jang Jinhee, Oh Se-Hong, Nam Yoonho, Jung Sehoon, Kim Sunhye, Masaki Fukunaga, Kim Woojun, Choi Hyung Jin, Lee Jongho, χ -separation: Magnetic susceptibility source separation toward iron and myelin mapping in the brain, 118371, Copyright 2021, with permission from Elsevier.* An imaging volume contains randomly distributed susceptibility sources in the voxel at the origin. The first column contains only paramagnetic (or positive) sources, the second column contains diamagnetic (or negative) susceptibility sources, and the third column is composed of paramagnetic and diamagnetic sources. The susceptibility sources induce magnetic field perturbation when B0 field is applied, making frequency shift in the imaging volume. Note that the frequency shift is zero when the same amount of para and diamagnetic susceptibility sources exist. Inside the voxel containing the susceptibility sources, transverse signal decay with irreversible (R_2) and reversible (R_2') decay occurs. Here, when both para- and diamagnetic susceptibility sources exist (3rd column), R_2' is the sum of the R_2' of the para- and diamagnetic sources.

(b) The frequency domain equation, magnitude domain equation, and combined model for χ -separation. D_f is the field perturbation kernel, and $D_{r,para}(\mathbf{r})$ and $D_{r,dia}(\mathbf{r})$ are the spatially varying relaxometric constant between R_2' and paramagnetic susceptibility, and between R_2' and diamagnetic susceptibility, respectively. The symbol * stands for convolution. Combining the magnitude and phase domain models, χ_{para} and χ_{dia} values are calculated by iteratively solving the minimization problem. In the current implementation of χ -separation, a nominal D_r is determined by linear fitting in deep gray matter ROIs. The same D_r is used for both sources disregarding the difference between $D_{r,para}(\mathbf{r})$ and $D_{r,dia}(\mathbf{r})$, and the spatial distribution of them. For reduction of streaking artifacts, optional regularization terms may be used, similar to QSM.

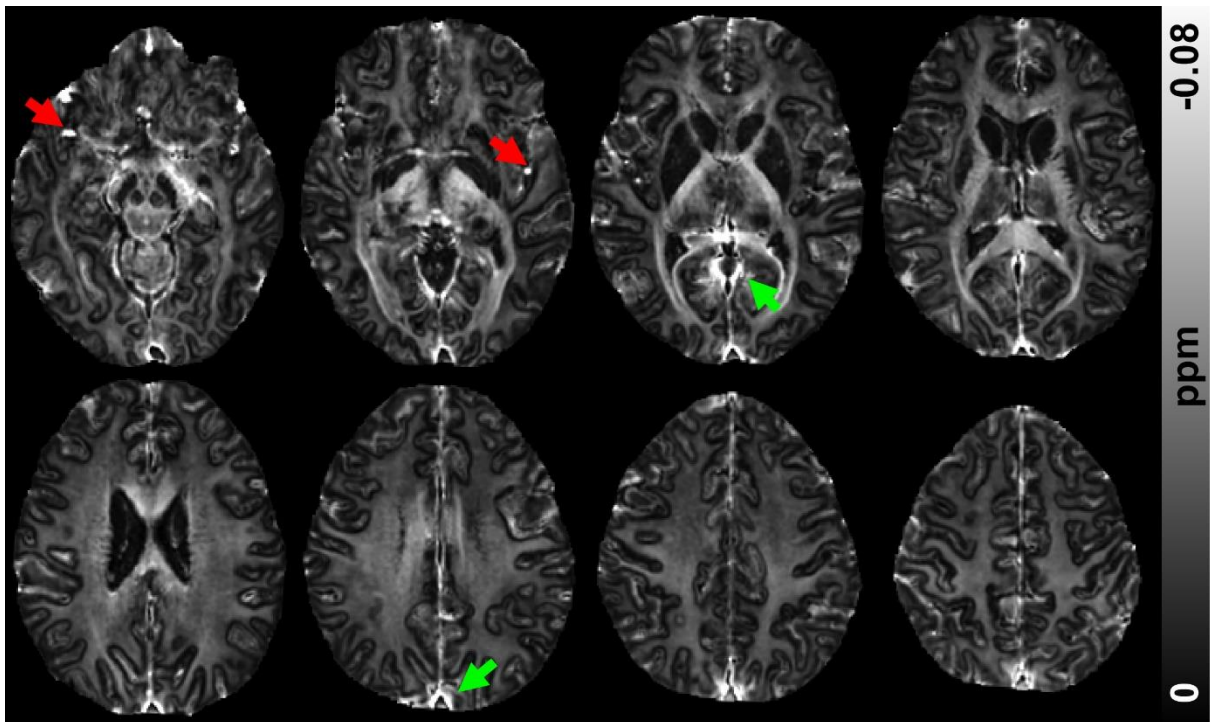


Figure 4. An example of a diamagnetic susceptibility map from a representative subject. Data were acquired at 3T with 0.75 mm isotropic resolution and field of view $192 \times 167 \times 120 \text{ mm}^3$ during the acquisition time of 5 min 51 sec. The diamagnetic susceptibility map was reconstructed using χ -sepnet- R_2^* that utilizes R_2^* instead of R_2' . The red arrows display the vessel-related artifacts, and the green arrows display the non-local R_2^* related artifacts.

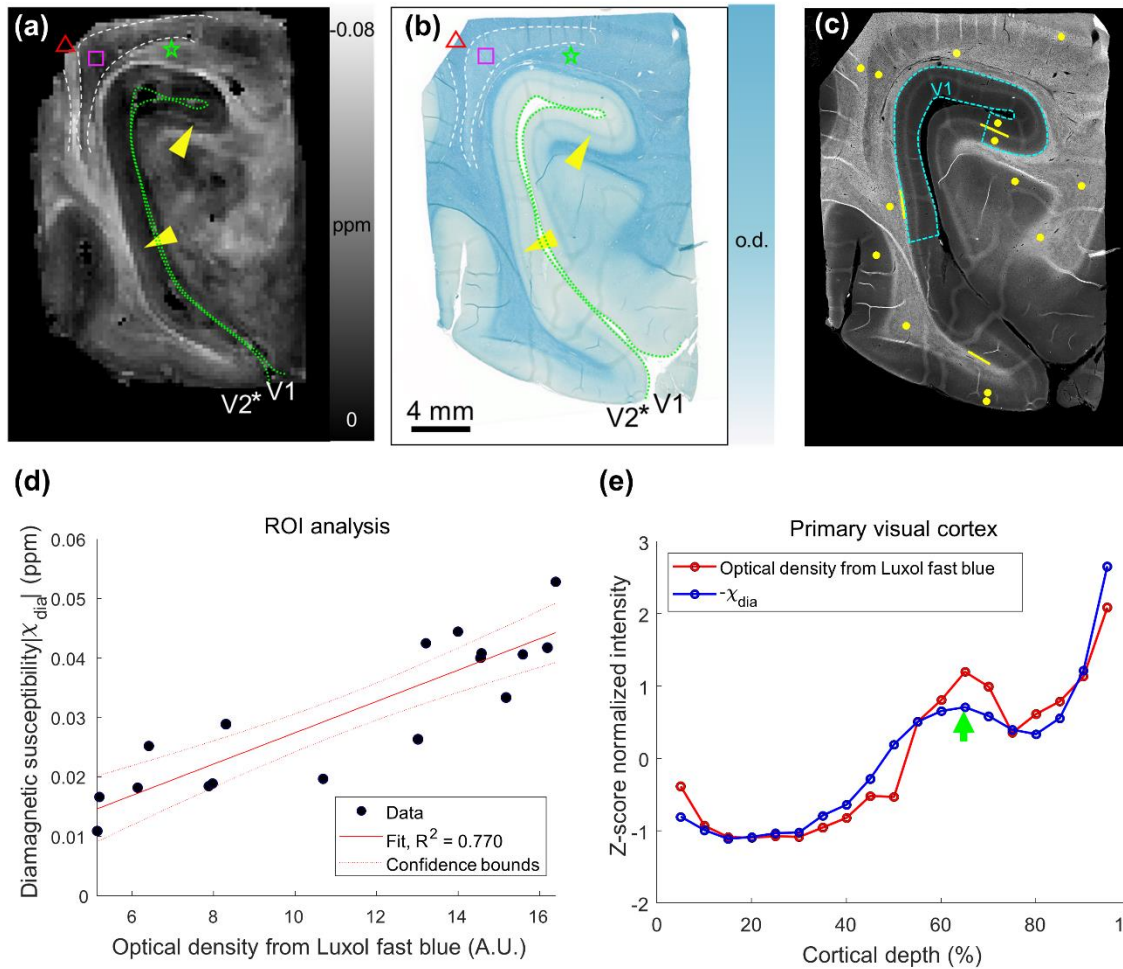


Figure 5 (a) A diamagnetic susceptibility map from χ -separation and (b) an LFB stained image. (a,b) are adapted and reprinted from *NeuroImage*, 240, Shin Hyeong-Geol, Lee Jingu, Yun Young Hyun, Yoo Seong Ho, Jang Jinhee, Oh Se-Hong, Nam Yoonho, Jung Sehoon, Kim Sunhye, Masaki Fukunaga, Kim Woojun, Choi Hyung Jin, Lee Jongho, χ -separation: Magnetic susceptibility source separation toward iron and myelin mapping in the brain, 118371, Copyright 2021, with permission from Elsevier. (c) The LFB stain image is converted to an LFB OD image for quantitative analysis. For an ROI analysis, 17 ROIs were chosen and drawn on each of the LFB OD and the diamagnetic susceptibility map. The ROIs are displayed as yellow circles and lines. (d) The ROI analysis result reveals good correlation between LFB OD and the diamagnetic susceptibility ($R^2 = 0.770$). (e) The cortical profiles of the diamagnetic susceptibility ($-\chi_{\text{dia}}$) and LFB OD from the primary visual cortex ROI (cyan dashed line in (c)). The two profiles agree, revealing the well-known mid-cortical laminar structure of the line of Gennari (green arrow).

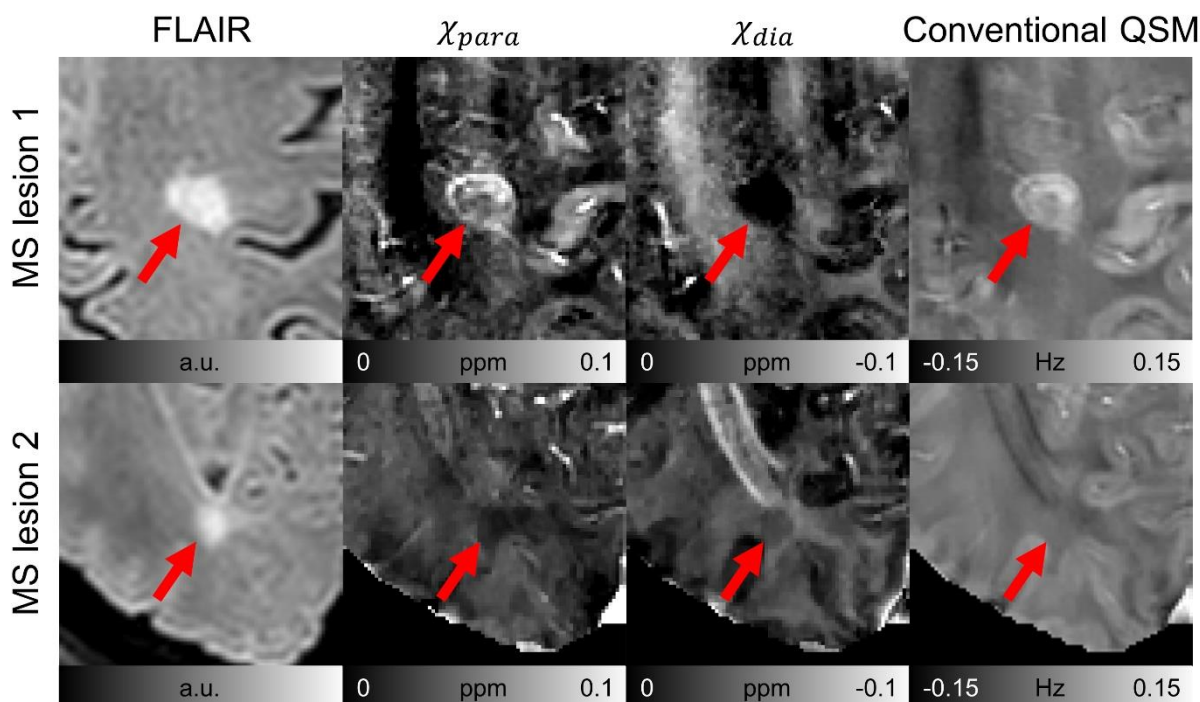


Figure 6. The in-vivo results of two characteristic MS lesions. *Adapted and reprinted from NeuroImage, 240, Shin Hyeong-Geol, Lee Jingu, Yun Young Hyun, Yoo Seong Ho, Jang Jinhee, Oh Se-Hong, Nam Yoonho, Jung Sehoon, Kim Sunhye, Masaki Fukunaga, Kim Woojun, Choi Hyung Jin, Lee Jongho, χ -separation: Magnetic susceptibility source separation toward iron and myelin mapping in the brain, 118371, Copyright 2021, with permission from Elsevier.* The red arrows indicate the MS lesions identified in the FLAIR images. The MS lesion in the first row displays a paramagnetic rim sign on both χ_{para} and conventional QSM maps. The χ_{dia} map suggests demyelination along with iron accumulation in the lesion, which cannot be identified using the conventional QSM. On the second row, the MS lesion displays low χ_{para} and χ_{dia} value, suggesting decreased iron and myelin. However, this lesion cannot be identified in the QSM map because both paramagnetic and diamagnetic susceptibility value has decreased, leading to isointense lesion in the QSM map.